Article

Quantum Dots Mediated Heterojunction coupling $MoSe_2$ Photoanode for Photoelectrochemical Water Splitting

Lin Zhang , Jiana Sun , Mengmeng Zhao , Yuxuan Wei , Taigang Luo , Zhengping Zhao * , Yibo Yan *

Posted Date: 16 January 2024

doi: 10.20944/preprints202401.1177.v1

Keywords: photoelectrochemical; hydrogen evolution; heterojunction; molybdenum selenide; quantum dot; photoanode; heteroatom doping

Article

Quantum Dots Mediated Heterojunction Coupling $MoSe_2$ Photoanode for Photoelectrochemical Water Splitting

Lin Zhang [1], Jiana Sun [1], Mengmeng Zhao [1], Yuxuan Wei [1], Taigang Luo [1], Zhengping Zhao [2,*] and Yibo Yan [1,*]

[1] Frontiers Science Center for Flexible Electronics (FSCFE), Xi'an Institute of Flexible Electronics (IFE) and Xi'an Institute of Biomedical Materials & Engineering (IBME), Northwestern Polytechnical University,127 West Youyi Road, Xi'an 710072, China; iamybyan@nwpu.edu.cn

[2] Zhijiang College, Zhejiang University of Technology, Hangzhou, Zhejiang 310014, China; sjzhaolei@163.com

* Correspondence: sjzhaolei@163.com; iamybyan@nwpu.edu.cn

Abstract: Graphene quantum dots (GQDs) possess the photosensitive absorption for photoelectrochemical hydrogen evolution owing to special band structures. Whereas they usually confront with photo-corrosion or undesired charge recombination during photoelectrochemical reactions. Hence, we establish the heterojunction between GQDs and $MoSe_2$ sheets via hydrothermal process for improved stability and performance. Photoanodic water splitting with hydrogen evolution boosted by heteroatom doped N,S-GQDs/$MoSe_2$ heterojunction has been attained due to the abundant active sites, promoted charge separation and transfer kinetics with reduced energy barriers. Diphasic 1T and 2H $MoSe_2$ sheets hybridized quantum dots contribute to the Schottky heterojunction, which can play a key role in expedited carrier transport to inhibit accumulative photo-corrosion and increase photocurrent. Heteroatom dopants lead to favored energy band matching, bandgap narrowing, stronger light absorption and high photocurrent density. The external quantum efficiency of doped heterojunction has been elevated twofold over that of the non-doped pristine heterojunction. Modification of graphene quantum dots and $MoSe_2$ heterojunction demonstrate a viable and adaptable platform toward photoelectrochemical hydrogen evolution processes.

Keywords: photoelectrochemical; hydrogen evolution; heterojunction; molybdenum selenide; quantum dot; photoanode; heteroatom doping

---

1. Introduction

Hydrogen evolution via photoelectrochemical (PEC) system has attracted numerous curiosities for sustainable clean energy transformation. The PEC catalysis often demands the appropriate electronic energy levels, bandgap structures and band edge positions. A series of metal oxides (e.g., TiO_2) were investigated as light harvester to absorb photons [1,2]. Nonetheless, the majority of metal oxides can only absorb partial simulated sunlight or visible light due to the large bandgap and short exciton lifetime due to the fast recombination of photogenerated carriers. For comparison, metal sulfides and nitrides have exhibited better electrical properties and more suitable bandgap structure for absorbing more visible light than metal oxides [3–7]. Additionally, graphene quantum dots (GQDs) have emerged as one of the hottest light harvesters with abundant active sites and bandgap suitable for photocatalytic and PEC applications [8,9], except for the inevitable charge recombination and photo-corrosion phenomenon. After coupling with appropriate cocatalysts, GQDs could largely promote the overall catalytic performance.

For improvement of the photostability, photocatalytic and photoelectrochemical activities of GQDs, surface modification such as grafting electron-donating functional groups and conjugating polyaromatic groups to enlarge π conjugation system have been employed in electronic energy bands engineering for hydrogen evolution and CO_2 reduction [10]. Intramolecular Z-scheme existed, consisting of p-type and n-type domains induced by electron-withdrawing and electron-donating species respectively, along with the sp^2-carbon ohmic contact in between. The Z-scheme configuration assisted to couple redox reactions averting the recombination of photogenerated electron-hole pairs. However, the yield of organic synthesis was complicated with side products. Facile synthesis was demanded with feasible and scalable operation processes. Heterojunctions between GQDs and various materials such as graphene, metal oxides and sulfides have been employed to improve photogenerated charge separation and inhibit recombination for elevated photoelectrochemical performance. GQDs and boron hybridized g-C_3N_4 heterojunction possessed ultrahigh specific surface area, enriched active sites, strong photoelectric activity and facilitated charge transfer ability [11]. Photocurrent was significantly enhanced by introduction of GQDs and boron in hybridized heterojunction than that of pure g-C_3N_4 nanosheets. Furthermore, the photocurrent linearly increased as dopamine concentration increased, showing high selectivity and stability for PEC detection of dopamine. Besides, GQDs could serve as the intercalation agent to exfoliate 2D materials such as graphene and form 0D/2D van der Waals heterojunction for PEC water splitting [8]. Heteroatom doping modified the bandgap structure, red-shift the photoluminescence (PL) and UV-vis light absorption wavelength spectrum for improved photogenerated charge separation, carrier transfer, PEC catalytic activity and reduced Schottky barrier on interface of the heterojunction.

Molybdenum selenide ($MoSe_2$) is a typical transition-metal dichalcogenide (TMD) material and frequently studied for the hydrogen evolution reaction (HER) [12,13]. Due to the favorable hydrogen adsorption energy, the $MoSe_2$ defective sites are taken as the catalytic active sites [14,15]. Subsequently, lots of studies have been focused on surface engineering of defects and active sites for enhancement of catalytic performance [16–18]. In photoelectrochemical catalytic HER, semiconductive 2H phase $MoSe_2$ efficiently improved the charge separation of photogenerated electron-hole pairs and stability [19,20]. However, the photogenerated charge separation and transfer were usually limited on the surface areas. To increase the catalytic effective surface area, exciton lifetime, facilitate photogenerated carrier separation and retard charge recombination, hybridization $MoSe_2$ with other materials were assembled to form heterojunctions to improve overall performance [21–23]. Micro/nanoflower heterojunction between $MoSe_2$ and g-C_3N_4 nanosheets facilitated the PEC faradaic efficiency and production yield of NH_3 formed by N_2. The elevated PEC performance was due to the hierarchical architecture, large effective surface area, abundant active sites, enhanced light absorption and improved charge separation by the hierarchical heterojunction structure [24]. Moreover, Z-scheme heterojunction photoanode of $MoSe_2$ nanosheets conjugated CdS-ZnO arrays exhibited high incident-photon-to-current efficiency and enabled the photoanode achieving high performance PEC hydrogen generation. The cooperation between tunable Z-scheme heterojunction with double internal electric fields and construction of 3D cross-linked network structure opened up a promising prospect for designing high-performance PEC water splitting devices [25]. In addition, partial conductivity also played a key role in determination of PEC catalytic performance. It was reported that core-shell heterostructure of (1T-2H) $MoSe_2$ on TiO_2 nanorods provided S-scheme heterojunction for charge separation and transfer in PEC catalytic activities for H_2O_2 production, where $MoSe_2$ could suppress the PEC decomposition of H_2O_2 by decreasing its adsorption by the photoanode surface. 1T $MoSe_2$ was quasi-conductive serving as the bridge between semiconductive 2H $MoSe_2$ and TiO_2 [26]. The 1T phase of $MoSe_2$ reduced the resistance / barriers and boosted charge transport kinetics, inducing dynamic improvement in PEC performance.

2. Results

2.1. Synthesis and Characterization

Hydrothermal synthesis of N,S-GQDs were implemented by using citric acid as the carbon source, urea as the nitrogen source and thiourea as sulfur source. 1 mmol citric acid, 3 mmol urea and 3 mmol thiourea were dissolved in 5 ml of deionized water, and sonicated for 10 minutes to dissolve uniformly and form a clear solution. Then transfer the solution to a 20 ml high-pressure autoclave and heat it in an oven at 160 ℃ for 4 hours. After the reaction was completed, it naturally cooled to room temperature to undergo continuous dialysis and freeze drying, the targeted product achieved

N,S-GQDs. For comparison, pristine GQDs were prepared similarly without using urea or thiourea as the N or S sources, respectively. Afterwards, quantum dots mediated $MoSe_2$ heterojunction was synthesized by another hydrothermal process of mixed two solutions: first, 4 mmol Se powder dispersed in 10 mL $N_2H_4 \cdot H_2O$, and second the 0.353 g $(NH_4)_6Mo_7O_{24} \cdot 4H_2O$ and 5 mg N,S-GQDs dissolved in 20 mL H_2O. The hydrothermal condition was set at 150℃ for 48 h to convert $Mo_7O_{24}^{6-}$ into Mo^{4+} for the $MoSe_2$ generation. The resulted sample was rinsed and centrifugated for 6 times to obtain the target heterojunction samples.

In Figure 1a, the transmission electron microscope (TEM) image of $MoSe_2$ nanosheets demonstrated that the stacked nanosheets consisted of around 3 to 8 monolayers. And the interlayer spacing is about 0.65 nm, corresponding to the interlayer spacing of 2H $MoSe_2$, indicating the existence of 2H phase $MoSe_2$ [23]. Interestingly, a triangular lattice structure (octahedral coordination) has been magnified and highlighted in the red box, with a lattice spacing of approximately 0.276 nm, which is close to the 1T phase (100) crystal plane spacing of $MoSe_2$ [22]. These results substantiated the existence of 1T phase and suggested the coexistence of 1T and 2H phases, where 2H phase is thermodynamically stable and 1T phase is much more conductive with higher electron density which has been caused by the highly reductive N_2H_4 agent. In addition, there are numerous defects on the basal plane and edge sites of $MoSe_2$, as indicated by the red circles, which may be ascribed to the lattice mismatching, resulting in a large number of internal and edge defects, and contributing to increased active sites. The high-resolution transmission electron microscope (HRTEM) of N,S-GQDs on $MoSe_2$ nanosheets were apparently observed in Figure 1b. Quantum dots smaller than 5 nm were evenly dispersed on surface of $MoSe_2$ nanosheets. The magnified HRTEM of red box area was exhibited in Figure 1c, showing periodic lattice arrangement with lattice spacing of 0.285 nm, indexed to the 2H phase (100) crystal plane spacing of $MoSe_2$. As indicated by the red circles, there are abundant defective vacancies, lattice mismatching and lattice disorders at the edge sites, which may increase the active sites and active surface areas. Energy dispersive spectroscopy (EDS) characterized elemental mapping has been shown in Figure 1d. Element distribution of C, N and S is mostly the same as that of Mo and Se, and the distribution is relatively uniform, which proves that N,S-GQDs are evenly dispersed on the $MoSe_2$ support. Selected area electron diffraction (SAED) pattern (Figure 1e) shows clear and highly symmetrical hexagonal or triangular pattern implying that the grown $MoSe_2$ nanosheets have hexagonal/triangular crystal structures. Scan electron microscopy (SEM) observation (Figure 1f) exhibited the relatively uniform size of nanosheets without obvious reaggregation toward large sheets. There are some curls on the edges, due to their relatively thin thickness and the decreased stiffness. To determine the thickness and number of atomic layers, the atomic force microscopy (AFM) analysis was performed (Figure 1g). The AFM results, consistent with the SEM and TEM results, demonstrate large layers and small fragments, showing quantum dots stacked on the $MoSe_2$ layers. The layer thickness is ranged from 4.6 to 5.4 nm. And the number of layers approximately ranged from 6 to 8, calculated based on the monolayer thickness of around 0.65 nm, and the additional distance induced by the influence of interatomic repulsion, capillary and adhesion forces.

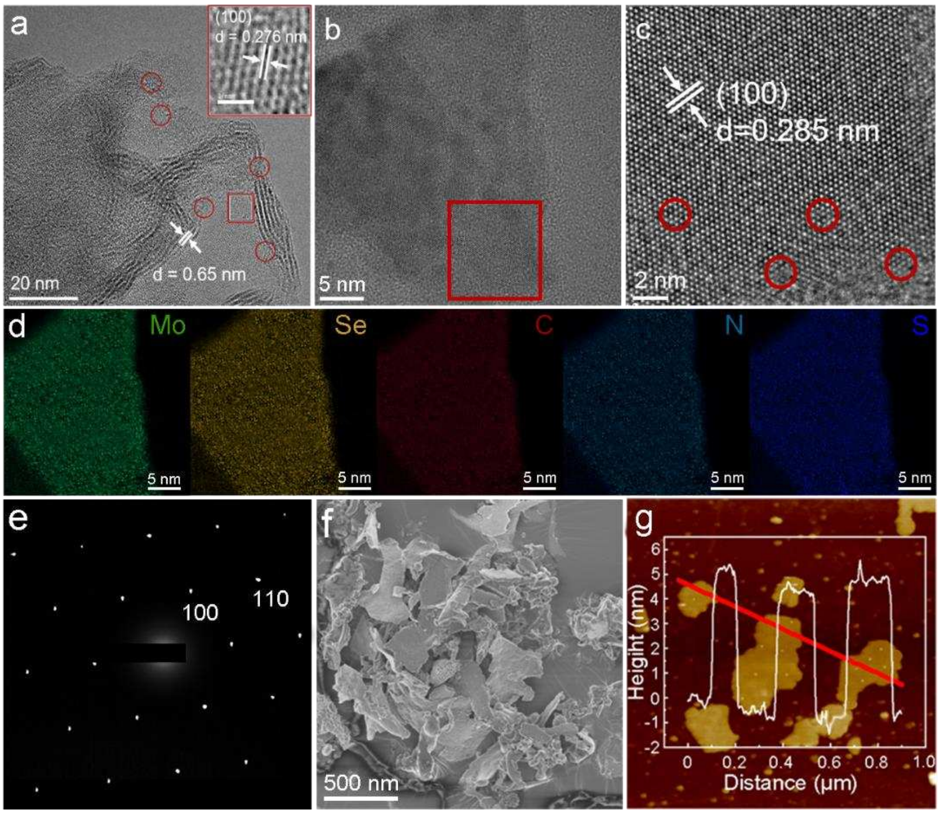

Figure 1. Structure characterizations (a) TEM, (b) HRTEM, (c) magnified HRTEM, (d) EDS mapping, (e) SAED, (f) SEM and (g) AFM of N,S-GQDs/MoSe$_2$.

The heterojunction structure of N,S-GQDs/MoSe$_2$ has been illustrated in Figure 2a. X-ray diffraction (XRD) spectra (Figure 2b) show two main diffraction peaks at 33.7 ° and 55 °, significantly differentiated from the standard PDF card of 2H phase MoSe$_2$ (JCPDs NO.29-0914). The two peaks at 33.7 ° and 55 ° are indexed to the (100) and (110) crystal planes, respectively. The small lattice spacing of 0.276 nm of 1T MoSe$_2$ corresponds to the (100) crystal plane peak (33.7 °) according to the Bragg law [27]. The Raman spectra in the range of 100-400 cm^{-1} were displayed in Figure 2c. The out of plane and in plane A_{1g} and E^1_{2g} vibration modes were observed at approximately 237 cm^{-1} and 281 cm^{-1}, respectively, attributed to the semiconductive 2H phase structure of MoSe$_2$. There is an in-plane B^1_{2g} vibration mode at around 335 cm^{-1}, attributed to the translational symmetry disruption occurring in the few layer MoSe$_2$ nanosheets [28]. In addition, there are some new Raman peaks located at 110 cm^{-1}, 148 cm^{-1}, 192 cm^{-1} and 375 cm^{-1}, labeled as J_1, J_2, J_3, and J_4 vibrational modes, respectively, attributed to the metal 1T phase of MoSe$_2$. The vibration modes of J_1, J_2, and J_3 are consistent with the Raman peaks of 1T-MoSe$_2$ prepared by Miao et al. [29], indicating good formation of 1T phase MoSe$_2$ nanosheets. Meanwhile, the J_4 mode has also been demonstrated in the report by Saghar et al [30]. Based on the analysis of Raman peak positions, it is further demonstrated that the hydrothermal synthesized MoSe$_2$ has a dual phase mixed structure of 1T and 2H. Figure 2d shows the overall XPS spectra of N,S-GQDs/MoSe$_2$, showing the coexistence of C, Mo, Se, N, and S elements, which is consistent with the results of EDS mapping. Figures 2d–i show the high-resolution XPS spectra of C 1s, Mo 3d, Se 3d, N 1s, and S 2p, respectively. The characteristic peaks located at 282.8 eV, 284.8 eV, 286.7 eV, and 288.6 eV in the C 1s XPS spectra are indexed to Mo-C, C-C, C-O, and C=O, respectively (Figure 2e). The presence of Mo-C bonds indicates that during hydrothermal reactions, N, S-GQDs form a certain number of covalent bonds with Mo^{4+}, contributing to the conductivity and active sites of the heterojunction. There are 5 characteristic peaks in the Mo 3d XPS spectra (Figure 2f), among which the characteristic peaks at binding energies of 229.1 eV, 232.3 eV, 230.5 eV, 233.7 eV, and 235.8 eV correspond to Mo^{4+} 3d$_{5/2}$, Mo^{4+} 3d$_{3/2}$, Mo^{5+} 3d$_{5/2}$, Mo^{5+} 3d$_{3/2}$, and Mo^{6+} 3d, respectively [31]. The presence of Mo^{5+} 3d$_{5/2}$, Mo^{5+} 3d$_{3/2}$, and Mo^{6+} 3d may be related to the incomplete reduction of Mo precursor $(NH_4)_6Mo_7O_{24}\cdot 4H_2O$. Interestingly, the binding energies of Mo^{4+} 3d$_{5/2}$ and Mo^{4+} 3d$_{3/2}$ shifted by ~0.9 eV compared to the standard binding energies of 2H $MoSe_2$ (Mo^{4+} $3d_{5/2}$ and Mo^{4+} $3d_{3/2}$ at 228.2 eV and 231.4 eV, respectively), implying that 1T $MoSe_2$ can engender from the hydrothermal method [32]. In Se 3d XPS spectra (Figure 2g), the characteristic peaks at 54.8 eV and 55.7 eV belong to Se^{2-} $3d_{5/2}$ and Se^{2-} $3d_{3/2}$, respectively, implying the −2 valence state of Se [33]. The N 1s XPS (Figure 2h) can be deconvoluted into four characteristic peaks at binding energies of 395 eV, 397.8 eV, 399.5 eV, and 401.5 eV indexed to the Mo 3p, Mo-N, pyrrolic-N, and graphitic-N, respectively. The presence of Mo-N indicates that N, S-GQDs, and $MoSe_2$ are not merely physically mixed, but also form Mo-N coordination bonds [34]. Graphene-N has been formed via substituting C atoms by N atoms. The S 2p XPS (Figure 2i) can be deconvoluted into four characteristic peaks, and the main S^{2-} $2p_{3/2}$ and S^{2-} $2p_{1/2}$ peaks are localized at 161 eV and 162.2 eV, respectively [35]. The characteristic peak at 164.8 eV indexed to the bridged disulfide S_2^{2-}, while the peak at 167.1 eV may be attributed to S^{4+}, caused by the incomplete oxidation of S^{2-}.

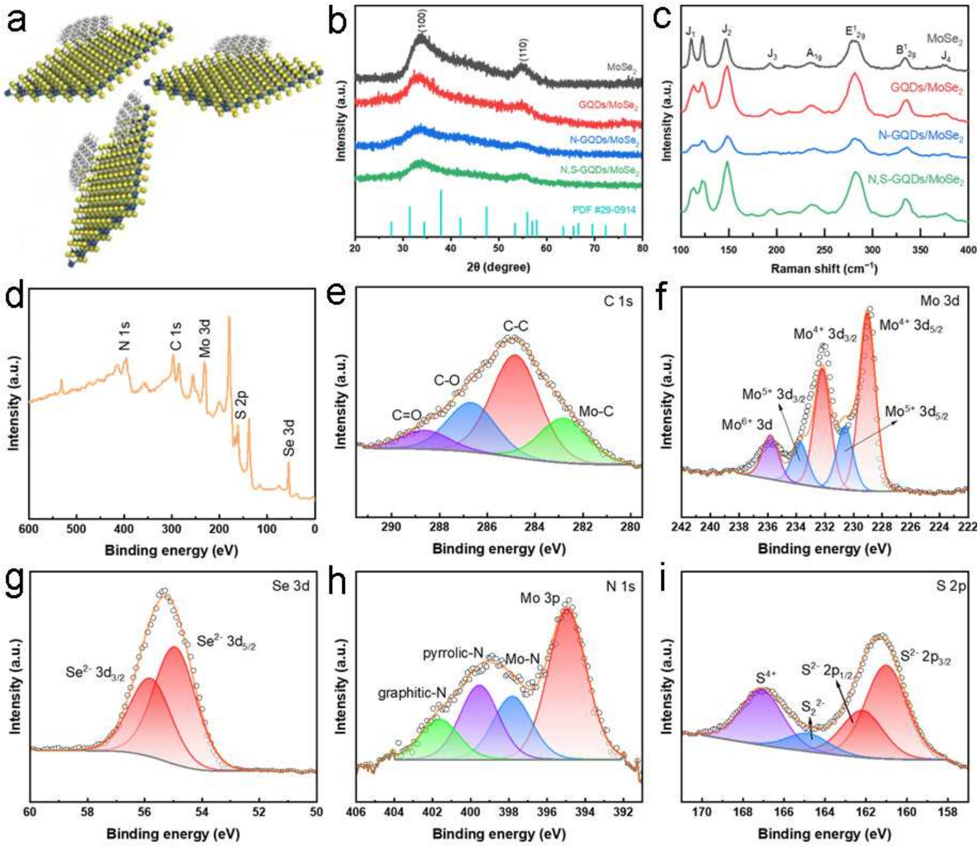

Figure 2. (a) Scheme of the heterojunction structure. (b) XRD, (c) RAMAN, (d) overall XPS, (e) C 1s, (f) Mo 3d, (g) Se 3d, (h) N 1s and (i) S 2p high resolution XPS patterns.

2.2. *Photoelectrochemical Performance*

The PEC performance was measured with a three-electrode system using 10%(v/v) lactic acid as electrolyte (pH=3). Linear sweep voltammetry (LSV) has been conducted to obtain polarized curves during the fourth cycle. Light on/off irradiation applied periodically chopped 1 sun (AM 1.5) at the intensity of 100 mW cm^{-2}, and photocurrent density was tested as the dependent variable of potential (Figure 3a). Negligible light-off currents indicate the high charge transfer resistance of the heterojunction samples, whereas the resistances can be dramatically decreased under light-on illumination, due to the high charge mobility and reduced diffusion resistance under light. The open-circuit potential (OCP) can be estimated by the potential values for zero photocurrent which was analyzed from the pattern of polarization curves. The OCP of the N,S-GQDs/$MoSe_2$ heterojunction was around −0.09 V vs RHE, while it is more negative at approximately −0.18 V vs RHE for non-doped GQDs/$MoSe_2$ heterojunction. The smaller negative value of OCP indicated fewer trapped

doi:10.20944/preprints202401.1177.v1

electrons in the N,S-GQDs/$MoSe_2$ heterojunction [36], when compared with GQDs/$MoSe_2$. And the N-GQDs/$MoSe_2$ is in between. It is worthwhile that the larger cathodic dark current of N,S-GQDs/$MoSe_2$ heterojunction at −0.20 V vs RHE, as the benchmark for the onset potential of HER, implying the occurring of HER. Positively sweeping the potential can afford large enough voltage to boost electrons to the counter electrode. The photocurrents of GQDs/$MoSe_2$ or N-GQDs/$MoSe_2$ exhibited faster saturation than N,S-GQDs/$MoSe_2$ heterojunction. The electrochemical impedance spectroscopy (EIS) has been performed with frequency ranged from 0.1 to 10^5 Hz (Figure 3b). Since both 2H and 1T phases coexisted in $MoSe_2$, specifically boosting the charge transfer for HER [37]. The semicircle diameters of the Nyquist plots were associated with charge transfer resistance (R_{ct}). The lowest R_{ct} of N,S-GQDs/$MoSe_2$ heterojunction implied the highest conductivity owing to the coexistence of 2H and 1T phases of $MoSe_2$ and the electron donating effects of N and S dopants. The low R_{ct} implied high charge transfer ability and long lifetime of the photogenerated electron-hole pairs, offering much improved photocurrent density. The chronoamperometric photocurrents were examined for analyzing the photo-response performance (Figure 3c). Periodic light on/off response were tested at 0.4 V vs RHE in electrolyte of 10%(v/v) lactic acid. Quick photo-responses were observed on anodes, with photocurrents rapidly recovered to saturation current in few seconds. Higher photocurrent of N,S-GQDs/$MoSe_2$ heterojunction was observed compared with GQDs/$MoSe_2$ or N-GQDs/$MoSe_2$ heterojunctions. The enhancement of the photocurrent in the heterojunction of the N,S-GQDs/$MoSe_2$ is attributed to the fast charge transfer within the system. N and S dopants can enhance the electron density with larger carrier concentration and better conductivity. Hydrogen evolution of N,S-GQDs/$MoSe_2$ heterojunction is over three times that of the GQDs/$MoSe_2$ under simulated sun irradiation (Figure 3d). The hydrogen production rate attained 4.91 μmol h^{-1} cm^{-2} at the apparent quantum efficiency of 7.62% under 420 nm irradiation. N and S dopants can favor the electron-donating and π-delocalization effects of the graphene quantum dots and lead to bandgap contraction, broadening the light absorption spectrum wavelength range. In the UV-visible light absorption spectra (Figure 3e), the light absorption abilities order as N,S-GQDs/$MoSe_2$ > N-GQDs/$MoSe_2$ > GQDs/$MoSe_2$. The inset exhibited PL spectra of quantum dots. N dopants introduce intermediate orbitals for electron transition and narrow the bandgaps. S dopants also introduce more orbitals, further donate and delocalize electrons to facilitate electron transitions together with narrower bandgaps. GQDs, N-GQDs and N,S-GQDs exhibit the PL emission centered at 540, 570 and 605 nm, corresponding to the bandgap of 2.30, 2.18 and 2.05 eV, respectively. Ultraviolet photoelectron spectroscopy (UPS) has been utilized to characterize the Fermi level and work function (Figure 3f). Work function (Φ) was calculated as the difference between the vacuum energy level (E_v) and the Fermi level (E_F), i.e.: $\Phi = E_v - E_F$. The Φ was determined by the energy difference between the electronic cutoff frequency energy (E_{cutoff}) and the excitation energy (21.2 eV). The Φ of $MoSe_2$ and N,S-GQDs were 4.6 and 4.2 eV, respectively. The band structure and charge transfer mechanisms of N,S-GQDs/$MoSe_2$ heterojunction was illustrated in Figure 3f inset. In addition, the distance between Fermi level and valance band maximum (VBM) of N,S-GQDs or $MoSe_2$ were tested from UPS in Figure S1 or S2 from Supplementary Material, respectively. Under light, the wavelength smaller than 605 nm (i.e., photon energy larger than bandgap energy 2.05 eV) can be absorbed, separate photogenerated electron-hole pairs and engender the photovoltage. Using a reverse bias can promote a minority of carriers driven toward the counter direction, inducing a photocurrent. Although high energy barrier at the interface did not favor significant photocurrents. The unique dual phases of $MoSe_2$ involving semiconductive 2H and metallic 1T could favor the carrier transport through energy- allowable pathways to the electrolyte. The photogenerated electrons rapidly transfer to the metallic 1T $MoSe_2$ and induce the hydrogen evolution reaction, while the photogenerated holes transfer via energetically favorable pathway on film, boosting the charge transfer kinetics and inhibiting recombination systematically. Much improved charge separation / transfer kinetics and suppressed recombination of N,S-GQDs/$MoSe_2$ in contrast to N-GQDs/$MoSe_2$ and GQDs/$MoSe_2$ has been evidenced by the photocurrent results, could provide a novel perspective to develop PEC catalysis for the hydrogen evolution reaction and various other applications.

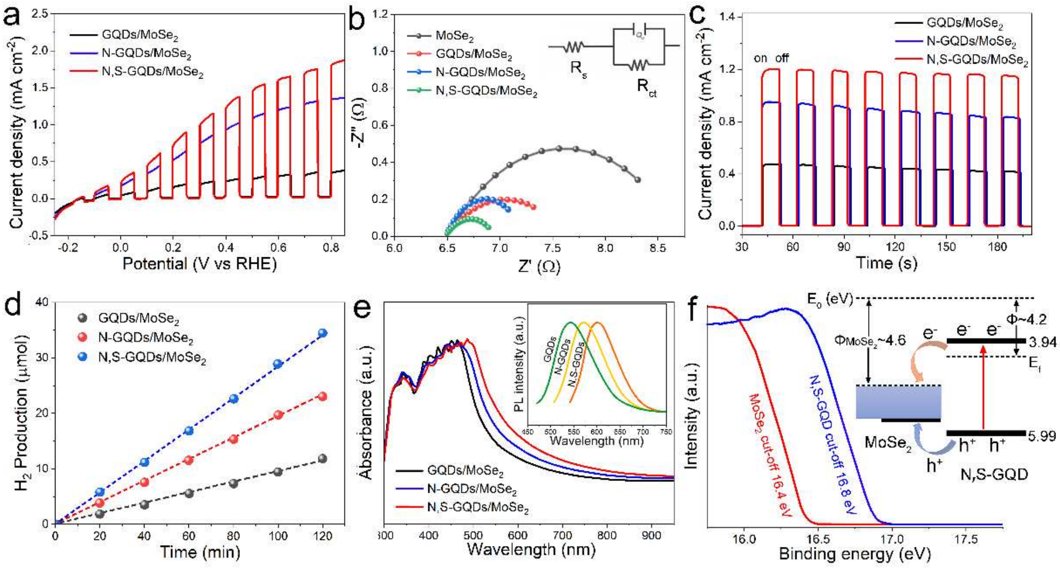

Figure 3. (a) Chopped current density–voltage measurements. (b) Nyquist impedance spectroscopy of different heterojunctions in the frequency range of 5 MHz to 10 Hz at a potential of 0 V vs RHE. (c) Photo-response measurement at applied voltage of 0.4 V in 10% lactic acid. (d) Photocatalytic H_2 generation. (e) UV–visible absorption spectra. Inset shows the photoluminescence of distinct quantum dots. (f) UPS spectra with inset for energy band alignment diagram.

3. Discussion

In general, the N,S-GQDs/$MoSe_2$ heterojunction has been prepared via hydrothermal synthesis with coexistence of metallic 1T phase and semiconductive 2H phase as a result of reductive $N_2H_4{\cdot}H_2O$ addition. For comparison, the N-GQDs and GQDs were prepared with only N dopants or non-dopants, respectively. The N and S dopants lead to reduced charge transfer barrier, bandgap narrowing, enhanced light absorption and photogenerated charge separation owing to the electron donating and delocalization effects. Coexistence of 1T and 2H phases $MoSe_2$ also contribute to rapid charge transfer, carrier transport and inhibit photogenerated charge recombination, improving the photocurrents and stability of the N,S-GQDs/$MoSe_2$ photoanodes in contrast to the N-GQDs/$MoSe_2$ or GQDs/$MoSe_2$ heterojunctions. This work offered new guideline to establish catalytic heterojunction system, especially surface mediation and bandgap engineering of heterojunctions, for PEC hydrogen evolution reaction and numerous other applications.

4. Materials and Methods

N,S-GQDs were hydrothermally synthesized by using citric acid as carbon source, urea as N source and thiourea as S source. Add 1 mmol citric acid, 3 mmol urea and 3 mmol thiourea into 5 ml deionized water, and ultrasonicated for 10 minutes to dissolve uniformly to form a clear solution. Then transfer the solution to a 20 ml high-pressure autoclave and heat it in an oven at 160 ℃ for 4 hours. Then, it was naturally cooled to room temperature to perform continuous dialysis and freeze drying, until the targeted product N,S-GQDs were achieved. In contrast, the N-GQDs were synthesized similarly without using thiourea as the S source. While, pristine GQDs were synthesized similarly without using urea or thiourea as the N or S sources, respectively.

Subsequently, heterojunctions between quantum dots and $MoSe_2$ were synthesized by another hydrothermal process of mixed two solutions: (1) 4 mmol Se powder dispersed in 10 mL $N_2H_4{\cdot}H_2O$ and (2) the 0.353 g $(NH_4)_6Mo_7O_{24}{\cdot}4H_2O$ and 5 mg quantum dots dissolved in 20 mL H_2O. The hydrothermal condition was set at 150 ℃ for 48 h to convert $Mo_7O_{24}^{6-}$ into Mo^{4+} for the $MoSe_2$ generation. The resulted sample was rinsed and centrifugated for 6 times to obtain the target heterojunctions (N,S-GQDs/$MoSe_2$, GQDs/$MoSe_2$ and N-GQDs/$MoSe_2$).

The morphologies of as-prepared samples were examined by transmission electron microscope (TEM, HT7700), high-resolution transmission electron microscopy (HRTEM, JEOL JEM-2100F), aberration-corrected high-angle annular dark-field scanning TEM (AC HAADF-STEM), and field-emission scanning electron microscope (FESEM, Hitachi SU-8010). The thickness of as-prepared catalysts has been measured measured by AFM (MultiMode of VEECO). The crystallinity structures of as-prepared heterojunctions were characterized by X-ray diffraction (XRD) technique (Empyrean 200895) using Cu Kα radiation. The chemistry environments of as-prepared samples were examined by X-ray photoelectron spectroscopy (XPS) spectra (Escalab 250Xi) with an Al Kα radiation. Surface work function was examined by UV-photoelectron spectroscopy (UPS, AXIS Ultra DLD) armed with the He-I photon source at hν of 21.2 eV. Raman spectra were measured by WITec (German), with the model number Alpha 300R and a wavelength laser emitter of 532 nm.

PEC water splitting was operated using three-electrode system with heterojunctions doped working electrode, saturated calomel electrode as the reference electrode and graphite rod as the counter electrode. The electrolyte of 10 % lactic acid was used to examine PEC performance. Light illumination employed simulated AM 1.5 using a Newport xenon lamp. Incident photon-to-electron conversion (IPEC) efficiency measurements have been operated by IQE 200TM (Newport) to investigate the photon wavelength-related photocurrent under monochromatic filtered light illumination as monochromator from a Newport 300 W xenon lamp. The H_2 was examined by gas chromatography (GC, Agilent 7890A) equipped with hydrogen flame ionization detector (FID) and thermal conductivity detector (TCD). Heterojunction photoanodes (2 x 2 cm^2) were applied in the quartz cell with electrolyte of 130 ml 10% lactic acid. This setup employed the three-electrode system using chronoamperometry technique at the bias of 0.4 V vs RHE.

Supplementary Materials: The following supporting information can be downloaded at the website of this paper posted on Preprints.org.

Author Contributions: Conceptualization, Y.Y. and L.Z.; methodology, L.Z.; software, W.T.; validation, Z.Z. and Y.Y. and L.Z.; formal analysis, J.S.; investigation, Y.Y.; resources, Z.Z.; data curation, T.L.; writing—original draft preparation, L.Z.; writing—review and editing, Z.Z.; supervision, Y.Y.; project administration, M.Z.; funding acquisition, Y.Y. All authors have read and agreed to the published version of the manuscript.

Funding: This research was funded by National Natural Science Foundation of China, grant number 62005216; and Basic Public Welfare Research Program of Zhejiang, grant number LQ22F050013.

Institutional Review Board Statement: Not applicable.

Informed Consent Statement: Not applicable.

Data Availability Statement: Data is contained within the article or supplementary material.

Acknowledgments: Authors acknowledge supports from the National Natural Science Foundation of China (62005216) and the Basic Public Welfare Research Program of Zhejiang (LQ22F050013).

Conflicts of Interest: The authors declare no conflict of interest.

References

1. Wang, M.; Sun, L.; Lin, Z.; Cai, J.; Xie, K.; Lin, C. p-n Heterojunction photoelectrodes composed of Cu2O-loaded TiO2 nanotube arrays with enhanced photoelectrochemical and photoelectrocatalytic activities. *Energy & Environmental Science* **2013**, *6*, 1211-1220.
2. Su, J.; Zhu, L.; Chen, G. Ultrasmall graphitic carbon nitride quantum dots decorated self-organized TiO2 nanotube arrays with highly efficient photoelectrochemical activity. *Applied Catalysis B-Environmental* **2016**, *186*, 127-135.
3. Tang, Z.K.; Tao, Y.; Wang, K.H.; Bao, D.Q.; Gao, Z.Q.; Zhao, H.G.; Zhang, H.; Wen, Z.; Sun, X.H. Lattice Mn2+ doped CdSe/CdS quantum dots for high-performance photoelectrochemical hydrogen evolution. *Nano Energy* **2023**, *113*, 108533.
4. Wang, W.H.; Jin, C.; Qi, L.M. Hierarchical CdS Nanorod@SnO2 Nanobowl Arrays for Efficient and Stable Photoelectrochemical Hydrogen Generation. *Small* **2018**, *14*, 1801352.
5. Wang, R.N.; Chen, S.B.; Ng, Y.H.; Gao, Q.Z.; Yang, S.Y.; Zhang, S.Q.; Peng, F.; Fang, Y.P.; Zhang, S.S. ZnO/CdS/PbS nanotube arrays with multi-heterojunctions for efficient visible-light-driven photoelectrochemical hydrogen evolution. *Chemical Engineering Journal* **2019**, *362*, 658-666.
6. Iqbal, N.; Khan, M.S.; Zubair, M.; Khan, S.A.; Ali, A.; Aldhafeeri, N.; Alsahli, S.; Alanzi, M.; Enazi, A.; Alroyle, T., et al. Advanced Photoelectrochemical Hydrogen Generation by CdO-g-C3N4 in Aqueous Medium under Visible Light. *Molecules* **2022**, *27*, 8646.

7. Mo, Z.; Xu, H.; Chen, Z.G.; She, X.J.; Song, Y.H.; Wu, J.J.; Yan, P.C.; Xu, L.; Leia, Y.C.; Yuan, S.Q., et al. Self-assembled synthesis of defect-engineered graphitic carbon nitride nanotubes for efficient conversion of solar energy. *Applied Catalysis B-Environmental* **2018**, *225*, 154-161.
8. Yan, Y.; Zhai, D.; Liu, Y.; Gong, J.; Chen, J.; Zan, P.; Zeng, Z.; Li, S.; Huang, W.; Chen, P. van der Waals Heterojunction between a Bottom-Up Grown Doped Graphene Quantum Dot and Graphene for Photoelectrochemical Water Splitting. *ACS Nano* **2020**, *14*, 1185-1195.
9. Wang, R.; Su, W.; Zhang, S.; Jin, L.; Zhang, J.; Bian, H.; Zhang, Y. Application of Lignin-Derived Graphene Quantum Dots in Visible Light-Driven Photoelectrochemical Photodetector. *Advanced Optical Materials* **2023**, *11*, 2202944.
10. Yan, Y.; Chen, J.; Li, N.; Tian, J.; Li, K.; Jiang, J.; Liu, J.; Tian, Q.; Chen, P. Systematic Bandgap Engineering of Graphene Quantum Dots and Applications for Photocatalytic Water Splitting and CO2 Reduction. *ACS Nano* **2018**, *12*, 3523-3532.
11. Zheng, L.; Zhang, H.; Won, M.; Kim, E.; Li, M.; Kim, J.S. Codoping g-C3N4 with boron and graphene quantum dots: Enhancement of charge transfer for ultrasensitive and selective photoelectrochemical detection of dopamine. *Biosensors and Bioelectronics* **2023**, *224*, 115050.
12. Wu, M.H.; Huang, Y.Y.; Cheng, X.L.; Geng, X.S.; Tang, Q.; You, Y.; Yu, Y.Q.; Zhou, R.; Xu, J. Arrays of ZnSe/MoSe2 Nanotubes with Electronic Modulation as Efficient Electrocatalysts for Hydrogen Evolution Reaction. *Advanced Materials Interfaces* **2017**, *4*, 1700948.
13. Yang, C.M.; Zhou, L.H.; Wang, C.T.; Duan, W.; Zhang, L.; Zhang, F.C.; Zhang, J.J.; Zhen, Y.Z.; Gao, L.J.; Fu, F., et al. Large-scale synthetic Mo@(2H-1T)-MoSe2 monolithic electrode for efficient hydrogen evolution in all pH scale ranges and seawater. *Applied Catalysis B-Environmental* **2022**, *304*, 120993.
14. Huang, L.; Wei, G.; Wang, J.; Li, D.; Jia, S.; Wu, S.; Jiang, T.; Guo, Y.; Liu, Y.; Ren, F. Ion Irradiation Activated Catalytic Activity of MoSe2 Nanosheet for High-Efficiency Hydrogen Evolution Reaction. *Advanced Energy Materials* **2023**, *13*, 2300651.
15. Nie, Z.; Xu, F.; Liu, H.; Wang, H.; Jiao, Y.; Zhu, W.; Wang, Q.; Yan, Y.; Zhu, J. Hierarchical heterostructure of vacant carbon-box erected MoSe2-x nanosheets as a functional mediator for high-performance lithium-sulfur batteries. *Chemical Engineering Journal* **2024**, *481*, 148433.
16. Song, Z.; Yi, J.; Qi, J.; Zheng, Q.; Zhu, Z.; Tao, L.; Cao, Y.; Li, Y.; Gao, Z.; Zhang, R., et al. Line defects in monolayer TiSe2 with adsorption of Pt atoms potentially enable excellent catalytic activity. *Nano Research* **2022**, *15*, 4687-4692.
17. Roy, K.; Maitra, S.; Ghosh, D.; Kumar, P.; Devi, P. 2D-Heterostructure assisted activation of MoS2 basal plane for enhanced photoelectrochemical hydrogen evolution reaction. *Chemical Engineering Journal* **2022**, *435*, 134963.
18. Kwon, I.S.; Kwak, I.H.; Kim, J.Y.; Debela, T.T.; Park, Y.C.; Park, J.; Kang, H.S. Concurrent Vacancy and Adatom Defects of Mo1-xNbxSe2 Alloy Nanosheets Enhance Electrochemical Performance of Hydrogen Evolution Reaction. *ACS Nano* **2021**, *15*, 5467-5477.
19. Zhu, C.; He, Q.; Sun, T.; Xu, M.; Wang, J.; Jin, Q.; Chen, C.; Duan, X.; Xu, H.; Wang, S. Edge-enriched laminar hexagonal (2H) MoSe2 -anchored sulfur vacancies-rich ReS2 nanoflowers for boosted light-to-hydrogen conversion. *Chemical Engineering Journal* **2023**, *464*, 142704.
20. Chung, Y.-J.; Yang, C.-S.; Lee, J.-T.; Wu, G.H.; Wu, J.M. Coupling Effect of Piezo-Flexocatalytic Hydrogen Evolution with Hybrid 1T-and 2H-Phase Few-Layered MoSe2 Nanosheets. *Advanced Energy Materials* **2020**, *10*, 2002082.
21. Li, Y.; Wang, M.; Sun, J. Molecular Engineering Strategies toward Molybdenum Diselenide Design for Energy Storage and Conversion. *Advanced Energy Materials* **2022**, *12*, 2202600.
22. Deng, S.; Yang, F.; Zhang, Q.; Zhong, Y.; Zeng, Y.; Lin, S.; Wang, X.; Lu, X.; Wang, C.-Z.; Gu, L., et al. Phase Modulation of (1T-2H)-MoSe2/TiC-C Shell/Core Arrays via Nitrogen Doping for Highly Efficient Hydrogen Evolution Reaction. *Advanced Materials* **2018**, *30*, 1802223.
23. Deng, S.; Zhong, Y.; Zeng, Y.; Wang, Y.; Yao, Z.; Yang, F.; Lin, S.; Wang, X.; Lu, X.; Xia, X., et al. Directional Construction of Vertical Nitrogen-Doped 1T-2H MoSe2/Graphene Shell/Core Nanoflake Arrays for Efficient Hydrogen Evolution Reaction. *Advanced Materials* **2017**, *29*, 1700748.
24. Mushtaq, M.A.; Arif, M.; Fang, X.; Yasin, G.; Ye, W.; Basharat, M.; Zhou, B.; Yang, S.; Ji, S.; Yan, D. Photoelectrochemical reduction of N2 to NH3 under ambient conditions through hierarchical MoSe2@g-C3N4 heterojunctions. *Journal of Materials Chemistry A* **2021**, *9*, 2742-2753.
25. Li, L.; Shi, H.; Yu, H.; Tan, X.; Wang, Y.; Ge, S.; Wang, A.; Cui, K.; Zhang, L.; Yu, J. Ultrathin MoSe2 nanosheet anchored CdS-ZnO functional paper chip as a highly efficient tandem Z-scheme heterojunction photoanode for scalable photoelectrochemical water splitting. *Applied Catalysis B: Environmental* **2021**, *292*, 120184.
26. Zhang, X.; Zeng, Y.; Shi, W.; Tao, Z.; Liao, J.; Ai, C.; Si, H.; Wang, Z.; Fisher, A.C.; Lin, S. S-scheme heterojunction of core–shell biphase (1T-2H)-MoSe2/TiO2 nanorod arrays for enhanced photoelectrocatalytic production of hydrogen peroxide. *Chemical Engineering Journal* **2022**, *429*, 131312.

27. Liu, D.; Wang, D.; Jing, X.; Zhao, X.; Xi, D.; Dang, D.; Meng, L. Continuous phase regulation of MoSe2 from 2H to 1T for the optimization of peroxidase-like catalysis. *Journal of Materials Chemistry B* **2020**, *8*, 6451-6458.
28. Wang, H.; Wang, X.; Wang, L.; Wang, J.; Jiang, D.; Li, G.; Zhang, Y.; Zhong, H.; Jiang, Y. Phase Transition Mechanism and Electrochemical Properties of Nanocrystalline MoSe2 as Anode Materials for the High Performance Lithium-Ion Battery. *Journal of Physical Chemistry C* **2015**, *119*, 10197-10205.
29. Jiang, M.; Zhang, J.; Wu, M.; Jian, W.; Xue, H.; Ng, T.-W.; Lee, C.-S.; Xu, J. Synthesis of 1T-MoSe2 ultrathin nanosheets with an expanded interlayer spacing of 1.17 nm for efficient hydrogen evolution reaction. *Journal of Materials Chemistry A* **2016**, *4*, 14949-14953.
30. Setayeshgar, S.; Karimipour, M.; Molaei, M.; Moghadam, M.R.; Khazraei, S. Synthesis of scalable 1T/2H–MoSe2 nanosheets with a new source of Se in basic media and study of their HER activity. *International Journal of Hydrogen Energy* **2020**, *45*, 6090-6101.
31. Zhao, Z.; Hu, Z.; Liang, H.; Li, S.; Wang, H.; Gao, F.; Sang, X.; Li, H. Nanosized MoSe2@Carbon Matrix: A Stable Host Material for the Highly Reversible Storage of Potassium and Aluminum Ions. *ACS Applied Materials & Interfaces* **2019**, *11*, 44333-44341.
32. Yu, Y.; Nam, G.-H.; He, Q.; Wu, X.-J.; Zhang, K.; Yang, Z.; Chen, J.; Ma, Q.; Zhao, M.; Liu, Z., et al. High phase-purity 1T'-MoS2- and 1T'-MoSe2- layered crystals. *Nature Chemistry* **2018**, *10*, 638-643.
33. Dai, C.; Qing, E.; Li, Y.; Zhou, Z.; Yang, C.; Tian, X.; Wang, Y. Novel MoSe2 hierarchical microspheres for applications in visible-light-driven advanced oxidation processes. *Nanoscale* **2015**, *7*, 19970-19976.
34. Guo, T.; Wang, L.; Sun, S.; Wang, Y.; Chen, X.; Zhang, K.; Zhang, D.; Xue, Z.; Zhou, X. Layered MoS2@graphene functionalized with nitrogen-doped graphene quantum dots as an enhanced electrochemical hydrogen evolution catalyst. *Chinese Chemical Letters* **2019**, *30*, 1253-1260.
35. Zhu, H.; Du, M.; Zhang, M.; Zou, M.; Yang, T.; Wang, S.; Yao, J.; Guo, B. S-rich single-layered MoS2 nanoplates embedded in N-doped carbon nanofibers: efficient co-electrocatalysts for the hydrogen evolution reaction. *Chemical Communications* **2014**, *50*, 15435-15438.
36. Krysa, J.; Zlamal, M.; Kment, S.; Brunclikova, M.; Hubicka, Z. TiO2 and Fe2O3 Films for Photoelectrochemical Water Splitting. *Molecules* **2015**, *20*, 1046-1058.
37. Wang, S.; Zhang, D.; Li, B.; Zhang, C.; Du, Z.; Yin, H.; Bi, X.; Yang, S. Ultrastable In-Plane 1T–2H MoS2 Heterostructures for Enhanced Hydrogen Evolution Reaction. *Advanced Energy Materials* **2018**, *8*, 1801345.